An experimentally-based friction law for high-velocity, long-displacement slip-pulse events during earthquakes

Zonghu Liao [a,b,c,*], Ze'ev Reches [b]

[a] *State Key Laboratory of Petroleum Resources and Prospecting, China University of Petroleum (Beijing), Beijing 102249, China*
[b] *School of Geology and Geophysics, University of Oklahoma, Norman, OK 73072, USA*
[c] *College of Geosciences, China University of Petroleum (Beijing), Beijing, 102249, China*

ARTICLE INFO

ABSTRACT

Large earthquakes initiate at small nucleation sites and propagate as rupture fronts along the host fault. It is inherently challenging to resolve the complexity of fault rupture at depth, and therefore, the evolution of frictional strength during earthquakes is commonly analyzed in laboratory experiments. We experimentally demonstrate here that this evolution depends simultaneously on all slip kinematic components: displacement, velocity and acceleration. We incorporate these components in shear experiments with slip-histories that resemble the theoretical expectations for earthquake slip. These experiments led to a new friction law that fits fault behavior during high-velocity/long-displacement slip. Our numerical simulations of dynamic rupture along a planar fault that obeys this friction law reproduced a range of earthquake source features including slip-pulse, Yoffe function, Gaussian velocity, and spontaneous slip arrest. Finally, we demonstrate that this experimentally-based friction law can realistically simulate the propagation and arrest of natural earthquakes.

1. Introduction

Many investigations have been devoted to the processes associated with fault slip during earthquakes (Scholz, 2002; Kanamori and Brodsky, 2004). A large earthquake initiates by local slip at a nucleation site followed by rupture propagates along the host fault (Fig. 1A). Understanding the rupture process is inherently challenging due to limited constraints on the conditions at earthquake depths (5-30 km), the attenuation of seismic waves, and the complexity of the rupture process. Therefore, fault behavior during natural earthquakes is investigated by experimental and theoretical analyses which demonstrated that fault resistance to slip depends on multiple, interrelated properties, including slip-kinematics, ambient stresses, temperature rise, fault-zone structure, and pore fluid properties (Brace and Byerlee, 1966; Ohnaka and Yamashita, 1989; Marone, 1998; Scholz, 2002; Kanamori and Brodsky, 2004; Hirose and Shimamoto, 2005; Tinti et al., 2005; Rice, 2006; Fukuyama and Mizoguchi, 2010; Sone and Shimamoto, 2009; Reches and Lockner, 2010; Di Toro et al., 2011; Chang et al., 2012; Svetlizky and Fineberg, 2014; Liao et al., 2014; Viesca and Garagash, 2015; Spagnuolo et al., 2016). Most of these properties, excluding slip-

kinematics, are poorly constrained for earthquake depth, making it difficult to utilize theoretical friction models for earthquake simulations. Further, the rupture front of a large earthquake imposes an extreme, non-linear, temporal loading that is difficult to simulate experimentally (Tinti et al., 2005; Reches and Dewers, 2005; Chang et al., 2012).

A typical earthquake is a rupture event that propagates at high-velocity along a fault with local rise-time periods from sub-second to a few seconds. Naturally, the slip-velocity history of such event includes an acceleration stage as the rupture front activates a resting fault patch, and a deceleration stage associated with the diminishing elastic energy. It is unlikely that a fault patch could reach a steady-state slip during such unstable, short-lived event. The total slip-displacement at a patch is the time integration of the slip-velocity history, which may differ from one patch to another as demonstrated by seismic inversion (Wald, 1996; Olsen et al., 1997; Ide and Takeo, 1997; Tinti et al., 2005). The expected slip-velocity history of a fault patch can be guided by a few conceptual models (Tinti et al., 2005; Liao et al., 2014) (Fig. 1B): (1) Yoffe model with infinite, initial acceleration followed by exponential deceleration (Tinti et al., 2005) (red, Fig. 1B); (2) 'Regularized Yoffe' model with intense, yet finite, initial acceleration (Tinti et al., 2005; Galetzka et al., 2015) (blue, Fig. 1B); (3) Gaussian model of symmetric velocity that initiates with increasing acceleration rate to a peak velocity followed by deceleration of similar style but inverted

* Corresponding author at: State Key Laboratory of Petroleum Resources and Prospecting, China University of Petroleum (Beijing), Beijing 102249, China.
E-mail addresses: zonghuliao@163.com (Z. Liao), reches@ou.edu (Z. Reches).
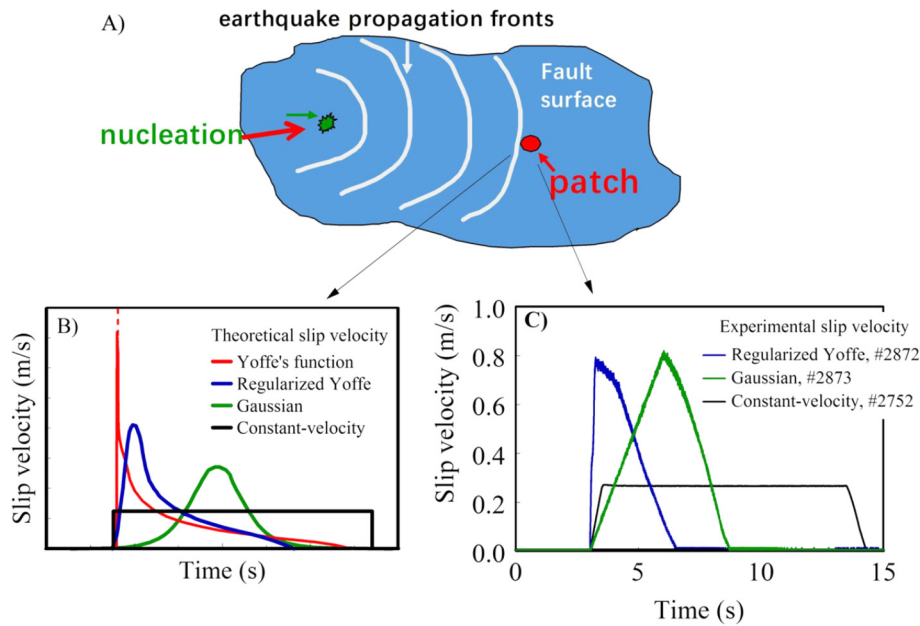
Fig. 1. Schematics of earthquake rupture. A, Main rupture zonation on a fault surface during a large earthquake. **B,** Conceptual models of the slip-velocity history during the rupture of a fault patch (after Tinti et al., 2005); axes not to scale. **C**, Experimental groups of slip-velocity history during high-velocity/long-displacement experiments along granite faults (Liao et al., 2014). Considering experimental limitations, these histories are regarded as proxies of the conceptual models in B. (For interpretation of the colors in the figure(s), the reader is referred to the web version of this article.)

sign (green, Fig. 1B); and (4) Constant-velocity model assumes no velocity change for slip duration (black, Fig. 1B). The actual velocity history at a specific patch will affect the evolution of local fault frictional strength that strongly depends on the slip kinematic components of slip-velocity (Chang et al., 2012; Marone, 1998; Fukuyama and Mizoguchi, 2010; Sone and Shimamoto, 2009; Reches and Lockner, 2010; Di Toro et al., 2011; Svetlizky and Fineberg, 2014; Liao et al., 2014), slip-displacement (Kanamori and Brodsky, 2004; Reches and Lockner, 2010; Di Toro et al., 2011), and slip-acceleration (Fukuyama and Mizoguchi, 2010; Chang et al., 2012; Liao et al., 2014). The slip-velocity of the theoretical Yoffe functions display non-linear, upward concave deceleration (Fig. 1B), yet to keep the experimental design simple, we use linear deceleration (see also Sone and Shimamoto, 2009). We discuss the effect of this choice later.

Bizzarri and Cocco (2003) recognized a difficulty in utilizing experimental observations for earthquake dynamic modeling. They stated: "There is a lack of experimental evidence confirming that these rate- and state-constitutive laws can be used to represent fault friction at high slip rates. The constitutive laws ... have been derived from laboratory stick-slip experiments in which the slip velocities are in the range of few microns to 10 mm/s ... Therefore we are confined to extrapolate the adopted constitutive laws at slip rates of the order of m/s as in real earthquake ruptures." The present analysis addresses this knowledge gap by developing a constitutive friction law at slip-velocities that are relevant to earthquake frictional slip.

We are guided by the indications that fault frictional strength depends on the three kinematic slip parameters: acceleration, velocity and displacement. These components are inherently linked to each other, e.g., slip-acceleration always invokes slip-velocity and slip-displacement. This linking implies that the evolution of fault frictional strength depends on the slip-velocity history. We derive here an experimentally-based friction law which incorporates the three kinematic components that control the dynamic strength of faults. We further argue that this law may effectively represent earthquake slip because slip-kinematics data are commonly determined by inversion of seismic observations (Wald, 1996; Olsen et al., 1997; Ide and Takeo, 1997; Tinti et al., 2005).

2. Experimental basis for a friction law

2.1. The search for a friction law suitable for earthquake slip

The well-known rate- and state-friction law (Dieterich, 1979; Marone, 1998), which fits well earthquake nucleation processes, was derived in experiments conducted at low slip-velocities (<1 mm/s) over short slip-distances (<10 mm). These kinematic values are orders of magnitude below the high-velocity/long-displacement conditions of large earthquakes (Bizzarri and Cocco, 2003; Di Toro et al., 2011). Another approach to defined a friction law includes utilization of high-velocity/long-displacement experiments conducted under constant slip-velocity (Di Toro et al., 2011; Reches and Lockner, 2010; Liao et al., 2014; Spagnuolo et al., 2016). However, these experiments do not incorporate the non-trivial history of slip-velocity during earthquake rupture that was determined is earthquake inversion analyses (e.g., Ide and Takeo, 1997; Tinti et al., 2005), and which is expected for slip-pulse behavior of earthquake slip (Heaton, 1990; Tinti et al., 2005). These limitations indicate the need for high-velocity/long-displacement experiments with slip-velocity history that simulates earthquake rupture as closely as possible. Similar experimental approaches were previously practiced without formulation of a friction law (Fukuyama and Mizoguchi, 2010; Chang et al., 2012; Liao et al., 2014), or used a modified rate- and state-friction law (Sone and Shimamoto, 2009).

The observational gap between low-velocity and high-velocity experiments was resolved for earthquake dynamic simulations by combining the classical rate- and state-law with intense frictional weakening at seismic slip-velocities (Bizzarri and Cocco, 2003; Noda and Lapusta, 2010; Jiang and Lapusta, 2016). While this practice of friction laws combination allows for earthquake rupture simulations, the combined laws are not based on experiments with slip-pulse history that naturally integrates the slip kinematic of acceleration, velocity and displacement. The central motivation of the present analysis is the derivation of a friction law that is based on direct experimental observations at high-velocity/long-distance conditions with continuous evolution of slip-pulse behavior.
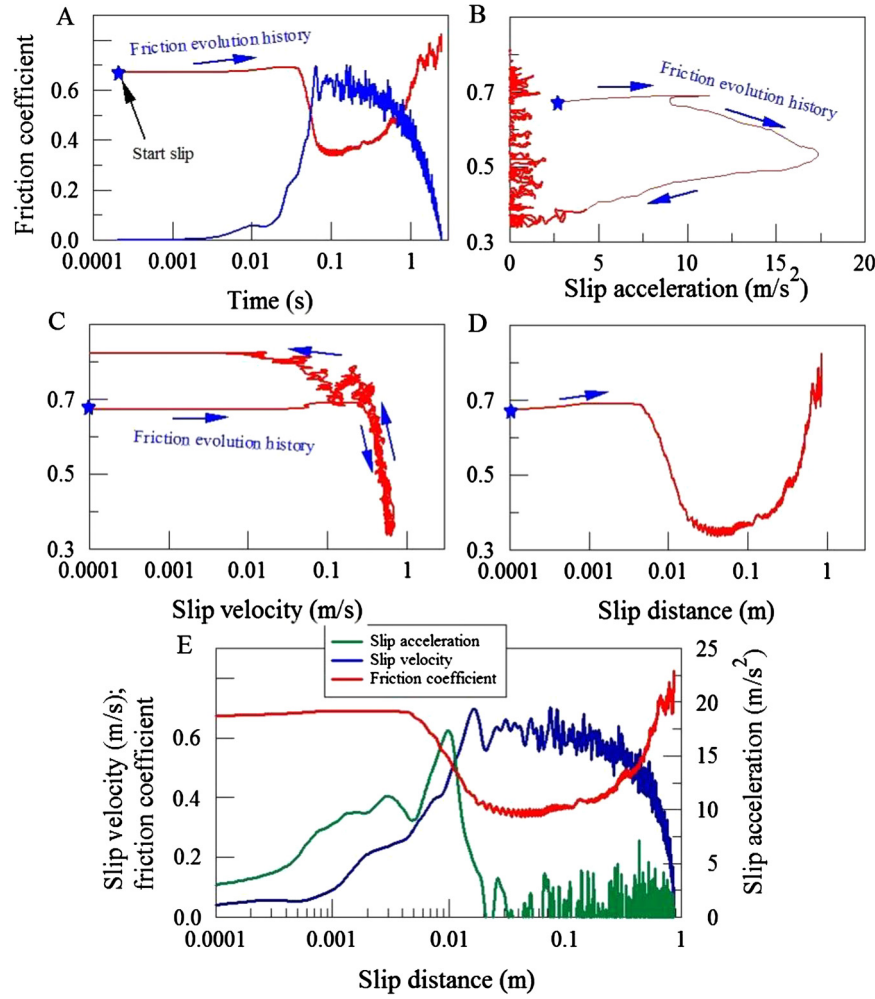
Fig. 2. Frictional strength evolution along granitic experimental fault that was sheared by spinning flywheel impact (**run 733 of Chang et al., 2012**). Measured friction coefficient as function of time (**A**), slip-acceleration (**B**), slip-velocity (**C**), and slip-distance (**D**). **E**, Friction coefficient, slip-acceleration and slip-velocity as function of slip-distance.

2.2. Friction law derivation

### 2.2.1. Experiments with non-trivial slip-history

The friction law derived here is based on two series of experiments that explored the effects of non-trivial slip history by shearing granite samples at velocity-histories (Fig. 1C) that resemble the conceptual models of earthquake rupture (Fig. 1B). The experimental setting is described in Appendix A and by Chang et al. (2012) and Liao et al. (2014).

Chang et al. (2012) developed an experimental procedure of abrupt, intense acceleration (green curve in Fig. 2E) followed by gentle deceleration. They used a rotary apparatus to shear granite samples at slip velocities up to 1.0 m/s, slip-distances up to 3.9 m, normal stress 2-7 MPa, and accelerations up to 50 m/s². The samples were impacted by a spinning massive flywheel (226 kg) that supplied a finite amount of energy. The impact of the experimental fault is viewed as analogous to impact of a natural fault patch by the earthquake rupture front, and the finite energy source is analogous to the finite elastic energy available for a natural earthquake. Chang et al. (2012) conducted 42 experiments on Sierra White granite at slip-velocities up to 1 m/s, and normal stresses up to 7 MPa.

Liao et al. (2014) used the velocity control capabilities of the apparatus to generate the three velocity histories of Fig. 1C. They conducted 43 experiments on granite samples using slip-velocities of $V = 0.0006$ to 0.23 m/s, and normal stresses up to 11.5 MPa. For the present analysis, we selected 16 of the above granite ex-

periments (Fig. 3) that represent the three types of slip-history defined in Fig. 1C: Regularized Yoffe (group 1), Gaussian (group 2), and constant velocity (group 3). To keep the experimental design simple, we use linear deceleration for the proxy of regularized Yoffe velocity (blue curve, Fig. 1C) whereas the theoretical Yoffe functions display non-linear deceleration (Fig. 1B); the effect of this choice will be discussed later. In the analyzed runs, the peak slip-velocity ranges $V = 0.10$ to 0.94 m/s, maximum acceleration ranges, $a = 3.2$ to 50 m/s², the normal stresses ranges, $\sigma_n = 2.0$ MPa to 6.8 MPa, and the total slip-distance from 0.04 m to 1.79 m. The measured parameters for these experiments are listed in Table A1.

The above shear experiments of Chang et al. (2012) and Liao et al. (2014) showed that the evolution and magnitude of the fault friction strongly depend on <u>all</u> kinematic parameters as well as the velocity-history. For example, an experimental fault made of Sierra White granite was subjected to a proxy of regularized Yoffe slip-history, including intense acceleration to peak velocity of 0.70 m/s in 0.06 s, followed by gentle deceleration to a cessation of slip in 2.44 s (Fig. 2A). The measured friction coefficient, $\mu = $ shear stress/normal stress, clearly depends on time, slip-acceleration, slip-velocity, and slip-distance (Fig. 2). Interestingly, the numeric simulations of earthquake slip by Bizzarri and Cocco (2003) also revealed simultaneous dependence of the frictional strength on both slip-velocity and slip-distance (their Fig. 3C).
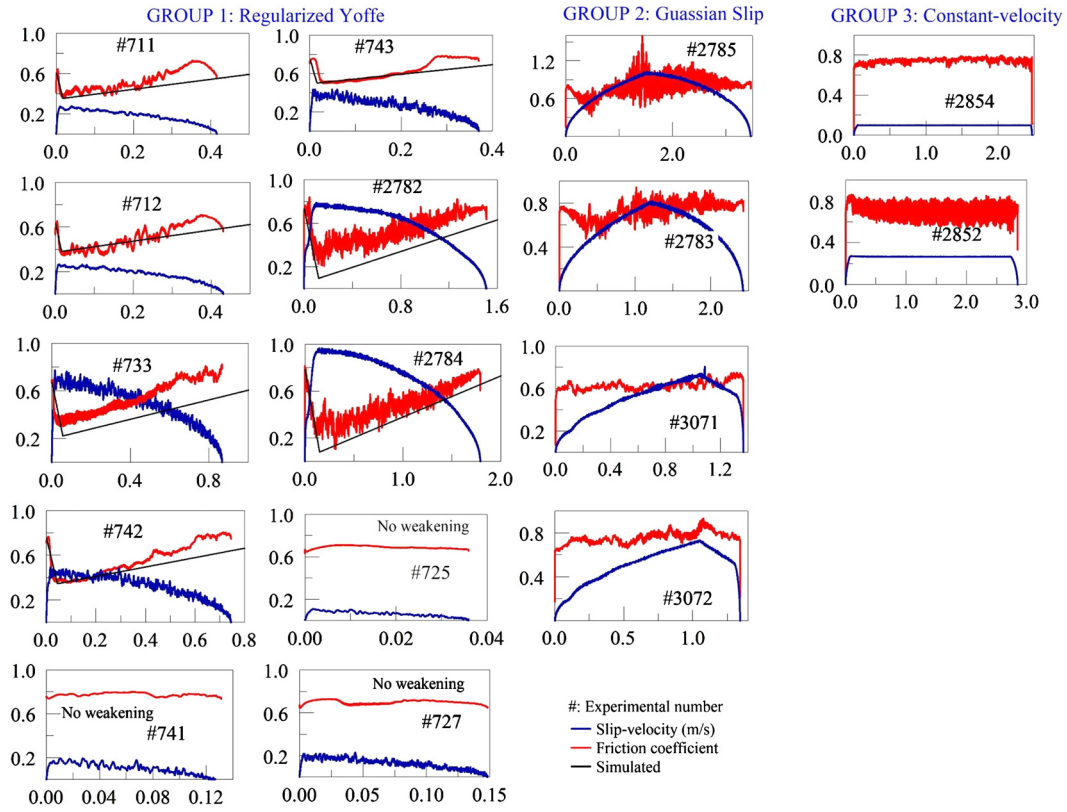
Fig. 3. The evolution of frictional strength during shear along experimental granite faults as function of slip-distance. Group 1: Eight runs out of 42 experiments with Sierra White granite loaded by flywheel (Chang et al., 2012), and two runs (#2782, #2784) out of 43 experiments with Red Radiant granite samples loaded by controlled slip-velocity (Liao et al., 2014). The selected runs cover the complete range of experimental loading intensities. Blue curves - slip-velocity; red curve - friction coefficient; both related to the scale on left side of the graphs; note difference of scales. These experiments (two left panels) are regarded as experimental proxy of regularized Yoffe function (Fig. 1B, see text). The black lines in the seven experiments with slip-pulse loading are the simulated friction evolution curves (equation (3) and Fig. 4); see text for discussion of fitting quality. Group 2: Experiments 2783 and 2785 were loaded by symmetric acceleration and deceleration and are considered as experimental proxies of Gaussian slip-history (Fig. 1C) and experiments #3071 and #3072 were loaded by proxies of reverse-Yoffe slip-history. Group 3: Experiments #2854 and #2752 were conducted at constant velocity.

2.2.2. Experimental observations

The analyzed runs (Fig. 3) (Table A1) display a few distinct features. In group 1, the seven runs with high acceleration and high peak velocity exhibit intense weakening, whereas the three experiments of lower acceleration and lower peak velocity (run #725, #727, #741 in Fig. 3) show no weakening (see Chang et al., 2012). This observation indicates that weakening the granite faults requires a slip-velocity and slip-acceleration that exceed a critical magnitude. Thus, we argue that friction law parameters which are suitable for dynamic slip simulations, must be determined in high slip-velocity and high slip-acceleration experiments. Runs of groups 2 and 3 that have low acceleration and/or low slip-velocity display no, or negligible weakening (Fig. 3). The goal of the present analysis is to derive a friction law suitable for earthquake frictional sliding, and therefore the following analysis focuses of runs of group 1 that better fit the expected (Tinti et al., 2005) and observed (Ide and Takeo, 1997) earthquake slip.

2.3. The 'History-Acceleration-Rate-Displacement' (HARD) friction law

2.3.1. The general formulation

The evolution of frictional strength in the above experiments (Chang et al., 2012; Liao et al., 2014) revealed three evolution stages (Fig. 2A, D, Fig. 3): A. Initial stage of gentle strengthening; B. Weakening stage with intense friction reduction that was associated with slip-acceleration; and C. Gradual strengthening stage associated with slip deceleration. We argue that these experimental procedures incorporate the relevant history for patch slip during earthquake propagation, and use the experimental results to formulate the 'History-Acceleration-Rate-Displacement' (HARD) friction law.

The HARD friction law considers the friction coefficient evolution as a function of slip-displacement, D (Fig. 4A). Following the experimental stages (Fig. 3), the friction coefficient, $\mu(D)$, evolves linearly in three stages (Fig. 4A): (1) During the initial strengthening stage, $\mu(D)$ increases from μ_0 (initial μ) to μ_S (peak μ) over slip displacement of D_H; (2) During the weakening stage, $\mu(D)$ decreases from μ_S to μ_K (lowest, kinematic μ) over slip displacement from D_H to D_W (weakening displacement) and (3) During the final, deceleration stage, $\mu(D)$ increases from μ_K to μ_F (final μ) over slip displacement from D_W to D_T (total slip displacement). The HARD formulation is,

$$\mu(D) = \begin{cases} \mu_O + (\mu_S - \mu_O) \cdot \frac{D}{D_H}, & D \leq D_H \\ \mu_S + (\mu_K - \mu_S)\frac{D-D_H}{D_W-D_H}, & D_H < D \leq D_W \\ \mu_K + (\mu_F - \mu_K)\frac{D-D_W}{D_T-D_W}, & D_W < D \leq D_T \end{cases} \quad (1)$$

Or in a general form:

$$\mu(D) = \mu_{i-1} + W_i(D - D_{i-1}) \quad (2)$$

in which $W_i = (\mu_i - \mu_{i-1})/(D_i - D_{i-1})$ defines the weakening or strengthening rate during various displacement stages. Equation (1) includes seven parameters that were measured in experiments (Fig. 3, Table A1). Later in the analysis, we determine the interrelationships between these parameters, and derive a simpler, working
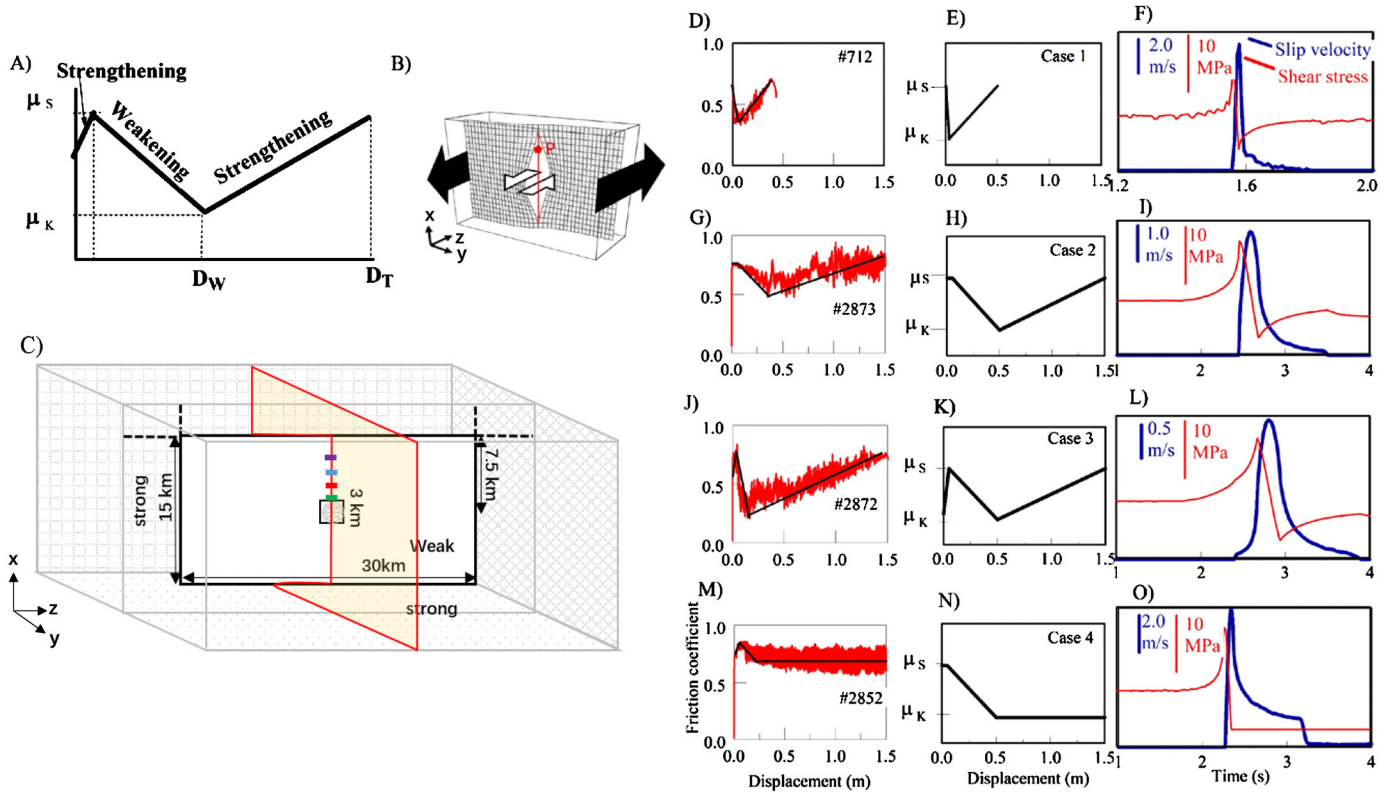
Fig. 4. Characteristics of 'history-acceleration-rate-distance' (HARD) friction law for experimental observations. **A**, Defined evolution of friction coefficient of HARD (equation (1) in text). **B**, The model of a crustal fault used in the dynamic rupture simulations with a vertical, infinitely long fault (Appendix B; Ampuero and Vilotte, 2002); open arrows - slip direction, black arrows - remote shear stress. The rupture propagates vertically from the origin to distances up to 7.5 km; rupture is monitored along x-axis, e.g., point P. **C**, Configuration of SCEC-USGS version 3 benchmark model for simulation of dynamic rupture along a strike-slip fault (Ampuero and Vilotte, 2002; Rojas et al., 2008; Barall and Harris, 2015). The line drawn through the origin indicates the monitoring points, green (1.5 km), red (3.0 km), blue (4.5 km) and purple (6.0 km) away from the nucleation patch. **D, G, J, M (left column)**, Friction coefficient and slip-velocity as function of slip-distance in four experimental cases (Chang et al., 2012; Liao et al., 2014) that represent as a range of fault behavior (text). **E, H, K, N (center column)**, HARD formulation of the four cases that idealize the experimental observations in D, G, J, M (text, data in Table A1). **F, I, L, O (right column)**, The simulated rupture characteristics of the four idealized cases in E, H, K, N; the simulations are for a fault that obeys HARD friction conducted with the setting of the model in **B** for benchmark mechanical (Appendix B; Tables A2, A3). The simulated results are shown for point P at $x = 6$ km. Red curves - fault shear stress; blue curves - slip-velocity; scales are marked.

formula that can be applied to both experimental data and field observations.

This friction law may resemble the classical, linear slip-weakening model (Ida, 1972; Palmer and Rice, 1973) that is commonly used in earthquake rupture simulations (Ampuero and Vilotte, 2002; Day, 2005; Weng and Yang, 2018). However, the HARD law is fundamentally different as it is based on high-velocity/long-displacement experiments with a slip-velocity history that inherently incorporates the simultaneous effects of all kinematic parameters (Fig. 2). The linear slip-weakening law, on the other hand, is based on constant velocity, steady-state experiments (e.g., Liao et al., 2014) that are not necessarily relevant to the acceleration/deceleration observed during earthquake slip.

We note that while the slip-velocity and slip-acceleration do not appear in equation (1), their values are manifested by the experimental parameters of slip-distance (D_H, D_W, and D_T) and friction-coefficient (μ_0, μ_S, μ_K, and μ_F). This situation is demonstrated by comparing two runs on the same granite sample. One run (#733, Fig. 2) has slip-acceleration of 28.8 m/s^2 and peak velocity of 0.7 m/s that yielded D_H, D_W, and D_T of 0.006, 0.047 and 0.87 m, respectively, and (μ_0, μ_S, μ_K, and μ_F of 0.670, 0.684, 0.34 and 0.810, respectively (Table A1). The run #725 (in Fig. 3), which has slip-acceleration of 8.3 m/s^2, peak slip-velocity of 0.1 m/s, and slip-distance of 0.036 m, displays only initial strengthening with $D_H = 0.005$ m and no weakening. It is clear that the kinematic intensities of this run were too low to trigger weakening and could not induce dynamic slip. Thus, the HARD formulation for

friction as function of slip-distance also encompasses the effects of slip-velocity and slip-acceleration in the selection of relevant high-velocity/long-displacement parameters.

2.3.2. The working formulation of HARD law

The general HARD formulation (equation (1)) has seven parameters that can be quantified by experimental measurements (Table A1). However, having so many independent parameters is not practical for the analysis of natural earthquakes. To derive a working formula of HARD, we first simplify the general law (equation (1)), and then explored for the intrinsic relations between the parameters in experiments with slip-history that resembles slip-pulse history (Fig. 1C). The central justification for this selection, is the widely accepted notion that slip during natural earthquake is dominated by slip-pulse rupture similar to regularized Yoffe model (Tinti et al., 2005; Galetzka et al., 2015).

We made here the following assumptions: (1) The initial strengthening stage (D_H) may be ignored as it occurs during the early loading that is likely due to apparatus acceleration limitation. Also, the observed D_H is small, frequently within the experimental resolution, e.g., in Table A1, the mean D_H is about 1/80 the mean D_T; and (2) The final friction coefficient, μ_F, equals the static friction coefficient, μ_S. For example, the mean values of μ_F and μ_S in Table A1 indicate that $\overline{\mu_F} = 1.02\,\overline{\mu_S}$. Using these assumptions indicate that the necessary HARD parameters are D_W, D_T, μ_S, and μ_K.
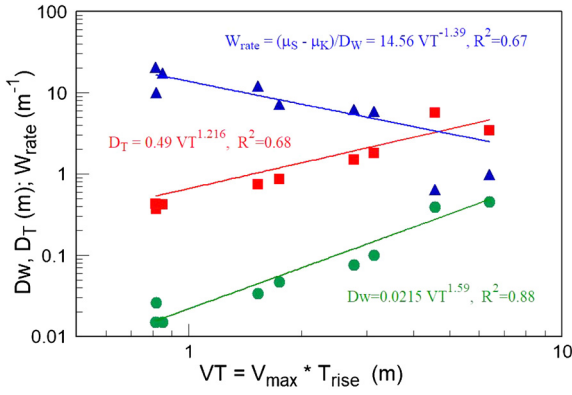
Fig. 5. Functional relationships of HARD parameters D_W, D_T, and W_{rate} with respect to VT for the first nine runs in Table A1 and shown in Fig. 3.

We searched for the interrelations between these four parameters in the nine experiments that display slip-history resembling slip-pulse configuration (the first nine experiments in Table A1 and the corresponding Fig. 3). We found that these parameters are related to the product of measured peak slip-velocity, V_{max}, and the measured rise-time, T_{rise}, defined here as $VT = V_{max} \cdot T_{rise}$. The calculated dependencies for the first nine runs with granite faults in Table A1 are the following functions (Fig. 5):

$$D_W = 0.0215 \cdot VT^{1.59} \quad r^2 = 0.88 \tag{3a}$$

$$D_T = 0.49 \cdot VT^{1.22} \quad r^2 = 0.68 \tag{3b}$$

$$(\mu_S - \mu_K)/D_W = 14.56 \cdot VT^{-1.39} \quad r^2 = 0.67 \tag{3c}$$

where D_W and D_T were defined in the general HARD formula (equation (1)) and $(\mu_S - \mu_K)$ is the friction coefficient drop during slip distance D_W; r^2 is root mean square error. We used the relations of equation (3a)–(3c)) to calculate the evolution of the friction-coefficient in the seven experiments with dynamic weakening based on the measured VT and static friction coefficient of each experiment. The calculated evolution histories, which are displayed by black lines in Fig. 3, are in very good agreement with the measured data (red curves) in terms of evolution trends and weakening distances. Yet, the calculated weakening intensity, $\mu_S - \mu_K$, slightly overestimates the experimental equivalent in three cases (# 2782, 2784, 733 in Fig. 3).

The existence of consistent relations between VT and HARD parameters in experiments with slip-pulse history has the promising potential to calculate the effective, local strength reduction for earthquake faults. This potential is based on the seismic analysis practice of derivation of the local peak slip-velocity, V_{max}, and associated rise-time, T_{rise}, by strong ground inversion (Wald, 1996; Olsen et al., 1997; Ide and Takeo, 1997; Galetzka et al., 2015).

3. Investigation and simulation of HARD friction law

3.1. Approach

We now investigate the effectiveness of HARD law in simulating the evolution of a rupture along a fault that is embedded within an elastic continuum (Fig. 4B). While we already simplified the HARD law (equations (3a)–(3c)), the simulations utilize the general formulation of HARD to investigate the sensitivity of the seven parameters. For the simulations, we used the space-time relations for rupture within an elastic continuum by Geubelle and Rice (1995) and Morrissey and Geubelle (1997):

$$V(x,t) = \left[\tau^0(x,t) - \tau(x,t) + f(x,t) \right] / \frac{G}{2c} \tag{4}$$

where $V(x,t)$ is the slip velocity, $\tau(x,t)$ is the shear stress on the fault plane, which is controlled by the friction law (HARD in present work), $\tau^0(x,t)$ is the remotely applied stress, G and c are the shear modulus and shear wave speed of the continuum, and $f(x,t)$ is the single convolutional function of the elastodynamic response of the continuum. These relations were previously employed to simulate dynamic rupture along faults with different frictional laws (Geubelle and Rice, 1995; Morrissey and Geubelle, 1997; Lapusta et al., 2000; Andrews, 1985; Day, 2005; Ampuero and Vilotte, 2002).

We implemented HARD friction law by substituting its components in the spectral boundary integral element code developed by Ampuero SBIEM (http://web.gps.caltech.edu/~ampuero/software.html). The simulations are for a vertical, planar fault embedded in a homogeneous elastic medium, with the mechanical properties (Fig. 4B) of the SCEC benchmark (Appendix B) (Fig. 4C, Tables A2, A3). The fault is 15 km long in the vertical direction (x), 30 km long horizontally (z), and subjected to horizontal shear loading (Fig. 4B). The rupture initiates at the nucleation region, which is stressed above the fault strength (Table A2), it propagates vertically up to 7.5 km away from the nucleation, and it is monitored at points along the x-axis (e.g., P, Fig. 4B). The results are described below in two parts.

3.2. Part I. Simulating rupture in four experiments

For the first series of simulations, we chose four experimental runs that display a spectrum of velocity history and associated friction evolution (Figs. 4D, G, J, M), and defined four classes of HARD law with friction evolution and total slip distance similar to the experimental observations (Figs. 4F, I, L, O). These HARD parameters were then applied in rupture simulations of SCEC benchmark (Appendix B, Table A2) while keeping all other crustal properties of the benchmark configuration. The evolutions of shear stress and slip-velocity of the four cases are presented for a point located 6 km above the center of the simulated fault (red point in Fig. 4B). Case 1 (Figs. 4D, E) has short displacement ($D_T = 0.5$ m) and fast weakening rate ($D_W = 0.033$ m) that led to a simulated Yoffe-type velocity function, short rise-time (~ 0.2 s), and short-lived rise-and-drop of shear stress (Fig. 4F). Case 2 (Figs. 4G, H) has long displacement ($D_T = 1.5$ m), and slow weakening rate ($D_W = 0.5$ m) that led to a simulated regularized Yoffe function, medium rise-time (~ 1.0 s), and shear stress rise-and-drop of ~ 1 s (Fig. 4I). Case 3 (Figs. 4J, K) has long displacement ($D_T = 1.5$ m), slow weakening rate ($D_W = 0.5$), and initial strengthening from $\mu_0 = 0.542$ to $\mu_S = 0.677$; these led to a simulated Gaussian velocity-history, long rise-time (~ 1.6 s), and shear stress rise-and-drop of ~ 1 s (Fig. 4L). Case 4 of $\mu_F = \mu_W$ (Figs. 4M, N) is the commonly used linear slip-weakening friction law (Ida, 1972; Palmer and Rice, 1973). Here (Fig. 4O), the simulated velocity-history resembles the truncated Kostrov function (Tinti et al., 2005), the rise-time is unbounded, and the shear stress rise-and-drop is short-lived. These simulations indicate that HARD formulation can be successfully incorporated dynamic rupture simulations to reproduce a wide range of slip-histories that are similar to the experimental observations.

3.3. Part II. Parameter investigation of HARD law

Part II of the simulations investigates the full range of HARD parameters for high-velocity/long-displacement events, namely (D_H, D_W, and D_T) and (μ_0, μ_S, μ_K, and μ_F). Our preliminary investigations indicated that the parameters of initial strengthening, D_H and μ_0, and the parameters that determining the weakening and strengthening rates, D_W and D_T, have a strong effect on the nature of the solutions. We thus explored four general classes that
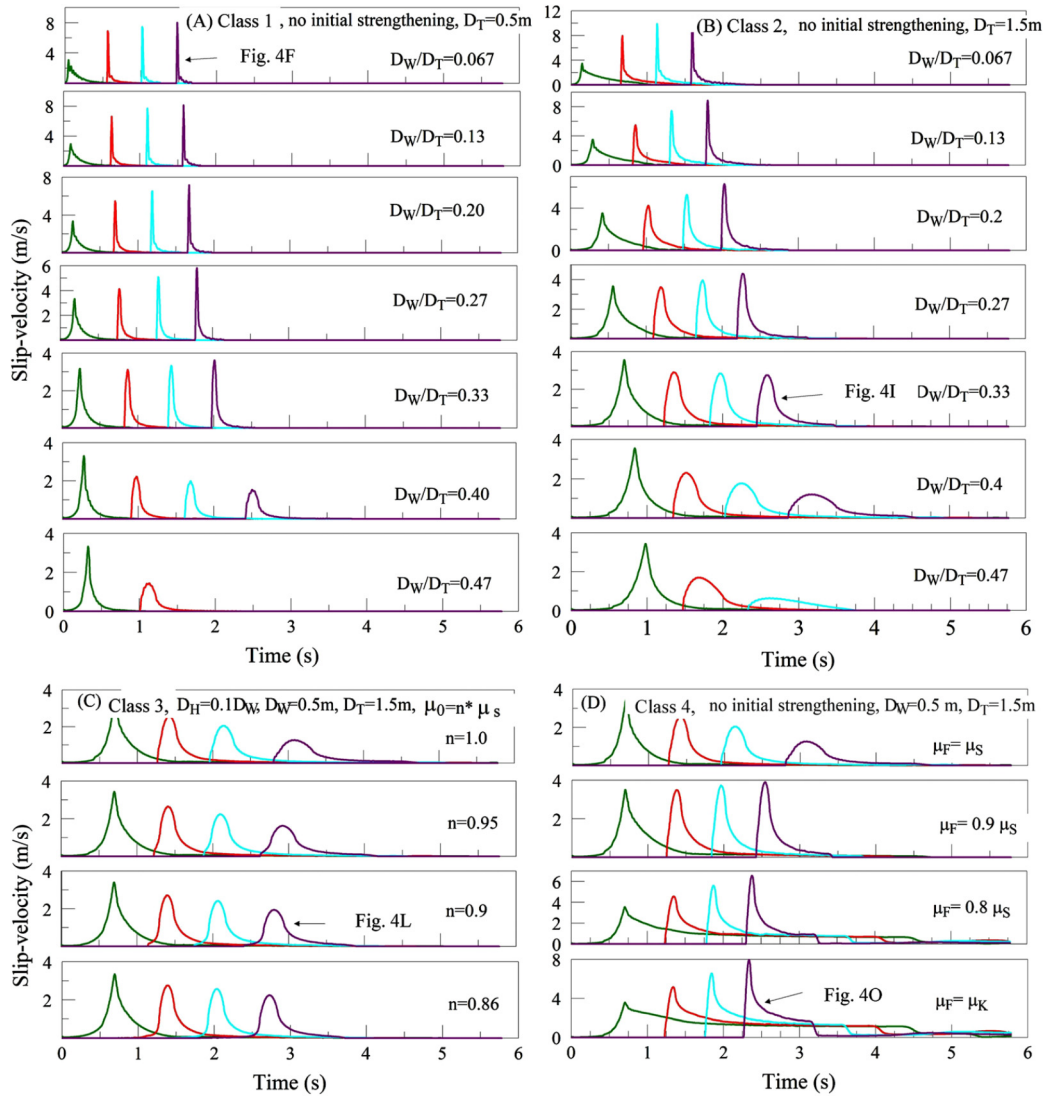
Fig. 6. Characterization of dynamic rupture along a vertical fault (Fig. 4C) with HARD frictional properties. The curves indicate the calculated slip-velocity history at four monitoring points away from the origin as shown in Fig. 4C: green at 1.5 km, red at 3.0 km, blue at 4.5 km, and purple at 6.0 km. The HARD parameters for these four classes are discussed in the text and listed in Table A3.

compare the SBIEM solutions for the HARD friction law by changing the four parameters above while keeping all other parameters constant. The used parameters are listed in Tables A2 and A3. The results are presented by the calculated slip velocity at four monitoring points located at distances of 1.5, 3.0, 4.5 and 6.0 km from the center of the nucleation patch (colored points in Fig. 4C). The plot for each simulation displays the rupture propagation velocity and the evolution of the slip-velocity with distance from the nucleation site. Note that the four cases of Fig. 4 were included in Fig. 6 as marked on the figures.

Class 1: Short-D_T and variable D_W. Fig. 6A displays the slip-velocity histories for fixed and short $D_T = 0.5$ m, and variable $D_W/D_T = 0.067$-0.47. The systematic trends of the rupture character with D_W/D_T are: (A) Increasing rise-time and decreasing peak-velocity with increasing D_W/D_T; (B) Reduction of rupture propagation velocity with increasing D_W/D_T; (C) Transition from Yoffe function to regularized Yoffe function with increasing D_W/D_T; (D) Increase of peak velocity with distance from the nucleation for $D_W/D_T < 0.33$, implying that the rupture will not be arrested spontaneously. In contrast, the simulations for $D_W/D_T > 0.33$ indicate systematic decrease of peak slip-velocity with distance that imply spontaneous arrest.

Class 2: Long-D_T and variable D_W. Fig. 6B for fixed, long $D_T = 1.5$ m displays slip-history variations with D_W/D_W that are generally similar to Class 1 with longer rise-times.

Class 3: Long-D_W and variable initial-strengthening. In this class, the parameters $D_W = 0.5$ m, $D_T = 1.5$ m, $D_H = 0.05$ m, are constant, and initial-strengthening rate, $\mu_0 = n \cdot \mu_S$, is changed where $n = 1.0$ to 0.86 (Fig. 6C). Here, the slip-history curves are symmetric, namely the Gaussian function (Fig. 1C). Note that the slip duration is finite at the four points.

Class 4: Long-D_W and variable final-strengthening. Time histories of Class 4 (Fig. 6D) correspond to the long-weakening stage (long D_W), and variable final-strengthening that is controlled by defining the μ_F relatively to μ_S and μ_K. The last model here is for $\mu_F = \mu_K$ is equivalent to the classical, linear slip-weakening friction law (Ida, 1972; Palmer and Rice, 1973; Andrews, 1985; Day and Dalguer, 2005). As expected, when μ_F decreases, the rupture velocity increases, for example, the point at 6.0 km distance (purple curves) is ~0.3 s faster is case of $\mu_F = 0.6$ than $\mu_F = 0.677$. Meanwhile, the maximum slip-velocity increases from ~1.5 m/s to ~4 m/s. When the $\mu_F = \mu_S$, the model shows an increase of peak velocity with higher rupture velocity. The rise time of the linear slip-weakening is larger than 3 s, which in the scale of the
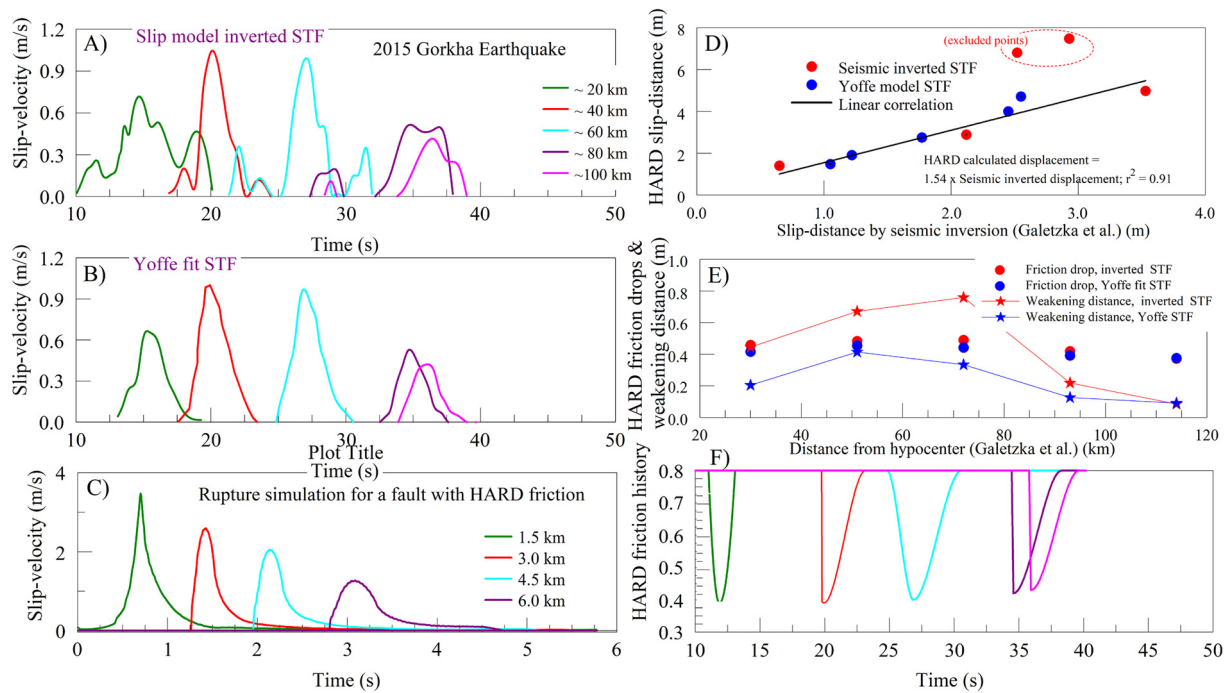
Fig. 7. Investigation of the 2015 M7.8 Gorkha earthquake, Nepal, with HARD law. A, Inverted slip-velocity history (STF) for five sub-faults of the 2015 Gorkha earthquake, Nepal (redrawn from Fig. 4 of Galetzka et al., 2015). The sub-faults are arranged along a line normal to the rupture front at the marked distances from the hypocenter. **B,** The Yoffe model fit to part of the inverted STF in A; redrawn from Fig. 4 of Galetzka et al. (2015). **C,** Slip-velocity history of simulated rupture along a fault with HARD friction; the velocity plot shown at four points at the marked distances from the origin (Fig. 4C); rupture calculation is for class 3, $n = 1$ (Fig. 6C). Note the qualitative similarity between **b** and **c** (text for details). **D–F** Application of HARD law (equations (3a)–(3c)) to the earthquake observations (text for details). **D,** Comparison between total slip-distance calculated by HARD, and the equivalent in the two versions of inverted STF at the five sub-faults; two marked outliners are excluded from the correlation. **E,** HARD calculated friction drops, $\mu_S - \mu_K$ (solid circles), and weakening distance, D_W (solid stars) for the two versions of inverted STF at the five sub-faults arranged at the distance from the hypocenter. **F,** The friction coefficient evolution at the five sub-faults according to HARD determined parameters in (D-E) for Yoffe fit STF results; $\mu_S = 0.8$ was assumed.

numerical model geometry (Fig. 6D) implies unbounded rise-time. In such case, the fault ruptures in crack mode instead of slip-pulse mode, and the ruptures "...do not arrest by themselves and propagate continuously" (Bizzarri and Cocco, 2003).

4. Application of HARD to Gorkha earthquake

We now apply the HARD friction law to analyze the frictional properties of the 2015 M7.8 Gorkha earthquake, Nepal, by using the seismic analyses of Galetzka et al. (2015) and Weng and Yang (2018). Galetzka et al. (2015) modeled "...the earthquake rupture as a slip pulse ∼20 kilometers in width, ∼6 seconds in duration, and with a peak sliding velocity of 1.1 meters per second, which propagated (horizontally) toward the Kathmandu basin at ∼3.3 kilometers per second over ∼140 kilometers." Galetzka et al. (2015) determined the Slip-rate Time Function (STF) during the earthquake slip by inversion of integrated seismic and GPS data, and used the resulting STF to evaluate the constitutive properties of the fault. The determined STF are presented for five sub-faults at distances between ∼30 km and ∼110 km from the hypocenter (their Fig. 4) that reveal local rise-time ranging from ∼5.5 s to ∼10 s (Fig. 7A). The analysis indicated rupture with ∼20 km wide slip-pulse (their Fig. 3A), and Galetzka et al. (2015) followed Tinti et al. (2005) to identify the part that fits the regularized Yoffe function of slip-pulse (Fig. 1B) in each of the five sub-faults (Fig. 7B). The resolved slip-pulse STFs (Fig. 7B) have the same maximum slip-velocity as the originally inverted STF (Fig. 7A), and shorter rise-times ranging ∼5.5-6.2 s. For the application of HARD law to Gorkha earthquake, we digitized the slip-velocity histories of Fig. 7A, B to calculate peak slip-velocity, V_{max}, and rise-time, T_{rise}, which were substituted in equations (3). The determined HARD parameters are applied below in a few steps.

In the first step, we compare the slip-velocity functions in Gorkha earthquake (Fig. 7A, B) and the slip-velocity histories in one HARD simulation that is displayed in Fig. 7C. This simulation was derived for class 3 in Fig. 6C with parameters $n = 1$ (Table A3). The simulation slip-velocities (Fig. 7C) and the earthquake inverted slip-velocities (Fig. 7A, B) share a few general features: (1) Distinct slip-pulse ruptures with finite rise-time; (2) Slip-velocity histories that are transitional between Yoffe and Gaussian velocity modes (Fig. 1B); and most importantly (3) A decrease slip-velocity with distance from the hypocenter that leads to spontaneous arrest. We note however that the HARD simulation at the first sub-fault displays the largest slip-velocity (green curve in Fig. 7C), whereas the seismic data (green curves in Fig. 7A, B) show a relatively small slip-velocity. This smaller velocity indicates slip-velocity increase from the hypocenter to its maximum level of ∼1 m/s at 40-60 km sub-fault. This dissimilarity between the simulation and observation could reflect the scale differences between the simulation (Fig. 4C) and the earthquake (Fig. 7A), the relative simplicity of HARD model, and the possible hybrid case of varied friction close to the hypocenter.

In the second stage, we apply the experimental parameters of HARD to the earthquake by using the maximum slip-velocity, V_{max}, and rise-time, T_{rise}, which were determined by Galetzka et al. (2015) (their Fig. 4B). We substituted the seismic data of V_{max} and T_{rise} into equations (3a)-(3c) to determine the friction characteristics at the five sub-faults, for the two types of STF: inverted (Fig. 7A) and Yoffe fit (Fig. 7B). Fig. 7D displays D_T, the total slip-distance (equation (3a)) as function of the seismic slip-distance of Fig. 7A, B. Excluding two outliers, the figure shows $D_T \approx 1.5 \cdot$ seismic slip-distance. This observation that the calculated D_T is larger than the seismic equivalent reflects the usage of maximum slip-velocity, which is about 50% larger than aver-

age slip-velocity. Next, Fig. 7E displays the calculated weakening parameters of weakening distance, D_W (equation (3b)), and the friction drop, $\mu_S - \mu_K$ (equation (3c)). The friction drop, $\mu_S - \mu_K$, for the two types of STF ranges 0.37-0.46, and the weakening distance is short: $0.08 < D_W < 0.8$ m. Finally, the calculated friction parameters, D_T, D_W, and $\mu_S - \mu_K$, are used to plot the expected evolution of the friction coefficient for the five sub-faults according to HARD constitutive law (assuming $\mu_S = 0.8$) (Fig. 7F).

In the above analysis, we applied the present observations of experimental slip-pulses under high-velocity/long-distance conditions to the seismic observations of slip-velocity and rise-time for the frictional properties during the Gorkha earthquake by Galetzka et al. (2015). The fault frictional properties which are associated this earthquake were also analyzed by Weng and Yang (2018) who used best-fit calculation of multiple dynamic simulations. Interestingly, while both analyses were based on the classical linear-weakening friction model, their results are significantly different. Galetzka et al. (2015) determined large weakening distance of ~5 m, whereas the best-fit solution of Weng and Yang (2018) is an order of magnitude smaller, ~0.5 m, that is in agreement with the present results of $0.08 < D_W < 0.8$ m (Fig. 7E).

5. Discussion

5.1. Friction control mechanisms of HARD model

The present derivations are based on the friction evolution during slip-pulse events in shear experiments. The underlying rationale is that fault behavior during such events is a non-trivial, simultaneous integration of multiple processes that are controlled by the loading conditions and system properties. As mentioned in the Introduction, the controlling features of the fault behavior include slip-kinematics, ambient stresses, rock type, temperature rise, fault-zone structure, pore fluid properties, and more. We selected the slip-kinematics as the controlling property for HARD derivations because it represents the rate of energy flux to the fault, and thus the slip-kinematics controls of temperature-rise and associated friction mechanisms. Further, many analyses moderate and large earthquakes evaluate the slip-kinematics by seismic inversion (e.g., Olsen et al., 1997; Galetzka et al., 2015; Weng and Yang, 2018), and thus facilitate the application of HRAD law. Finally, the HARD law is formulated by the evolution of the friction coefficient with slip-distance without considering the experimentally applied slip-velocity (Figs. 1C, 4). Yet, using this law in dynamic simulations (e.g. in Fig. 4E, H) generated slip-velocity histories (Fig. 4F, I) that strongly resemble the theoretical Yoffe functions (Fig. 1B). This similarity between the theoretical and simulated velocity evolution indicates that in both frameworks the slip-velocity is controlled by the energy within the elastic solid.

We envision that a slip event would activate the following physical processes during the three main stages of the slip-pulse (Fig. 1).

a. The intense acceleration stage is affected by the earthquake rupture front that imposes an extreme, non-linear, temporal loading (Tinti et al., 2005; Reches and Dewers, 2005; Svetlizky and Fineberg, 2014). This loading causes intense fragmentation and pulverization (Wilson et al., 2005; Reches and Dewers, 2005), and the fast pulverization accelerates the fault weakening and generates a fresh gouge layer ready for the high-velocity stage (Wilson et al., 2005; Chang et al., 2012).

b. Fault weakening processes during high-velocity slip ($V > 0.5$ m/s) were studied in many steady-state analyses that revealed multiple effective mechanisms that are commonly thermally controlled. These mechanisms include melting (Hirose and Shimamoto, 2005; Chen et al., 2017b), flash heating (Goldsby and Tullis, 2011), phase transformation (Di Toro et al., 2004; Han et al., 2007; Green et al., 2015), power lubrications (Reches and Lockner, 2010), and nanoparticle smoothing (Chen et al., 2013). These mechanisms are not directly applied to numerical simulation due to their inherent complexity.

c. Fault strengthening during deceleration from high-velocity slip (Figs. 2, 3) was investigated systematically only in a few experimental works. Reches and Lockner (2010) demonstrated profound fault strengthening when slip-velocity decreases (their Fig. 4), and this time-dependent strength recovery of the fine-grained gouge was attributed to grain agglomeration, sintering, and destruction of powder-rolls (Chen et al., 2017a). The fault mirrors along carbonate faults are destroyed during low-velocity stages leading to significant strengthening (Siman-Tov et al., 2015).

5.2. Stability analysis

The stability of steady state frictional sliding is investigated generically by a critical length scale as previously discussed (Ampuero and Vilotte, 2002; Dascalu et al., 2000). The instability involves a critical size, h^*, which can be obtained by:

$$h^* \approx \frac{\pi G D_W}{\tau_n(\mu_s - \mu_K)} \tag{5a}$$

$$\Delta t = \beta \Delta x / c \tag{5b}$$

in which G is shear modulus, $\tau_n(\mu_s - \mu_K)$ is an expression restricted to the stress drop, and D_W is regarded as the critical slip distance. This approach attempts to make the element size, h, smaller than the critical size, h^*, thus to insure the perturbation on a single cell is only a part of larger space segment. We use this approach by considering a maximum solution of h^* as 182 m for $D_W = 0.033$ and 2757 m for $D_W = 0.5$ m. For the case of initial strengthening, h^* is calculated to be 206 m for $D_H = 0.05$ m. The cell size is selected as 2.08 m in this study and the model produces stable results. Our computations show that the histories of velocity converge to each other through changing the grid sizes qualitatively. For the time resolution, we use $\beta \min = 0.5$ and the time step, Δt, is determined by equation (5). The time step of 0.01 s is selected so that slip in a time step does not exceed a fraction of the characteristic slip distance determined by HARD slip weakening distance D_W. The exact critical size at extreme cases has been computed and discussed (Dascalu et al., 2000).

6. Summary

The HARD friction law is based on shear experiments that resemble dynamic rupture, the law is easily incorporated in earthquake dynamic simulations, and it is powerful in producing the wide range of the expected, yet unknown, modes of earthquake rupture. We thus envision that numerical simulations with this friction law, when incorporated with the local crustal properties would succeed to quantitatively reproduce natural earthquakes features, including self-healing slip pulses, spontaneous arrest, rise-time and ground shaking.

Acknowledgements
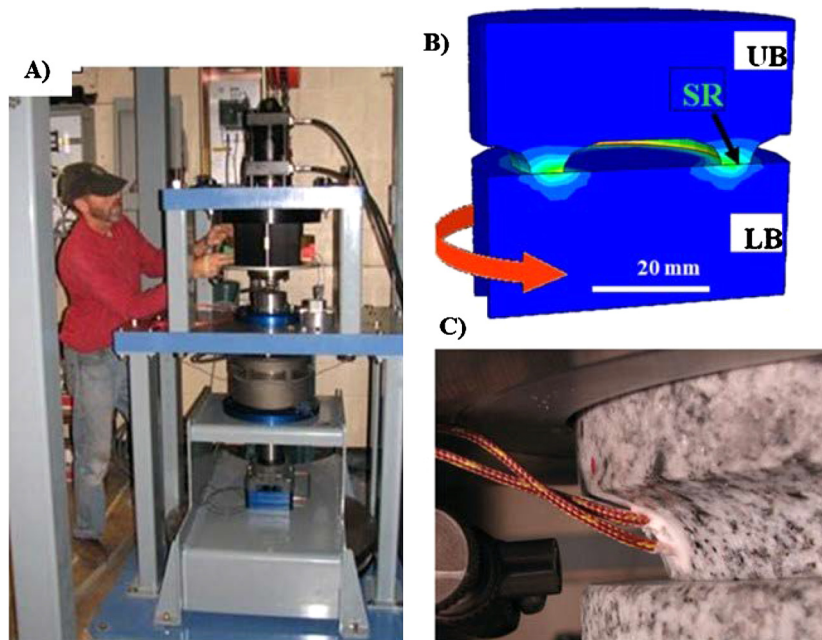
Fig. A1. The Rotary Shear Gouge Apparatus (ROGA). A, General view; note from bottom to top: massive flywheel (below the gray base, and seen on both sides of the base), vertical power shaft, electromagnetic clutch, central deck where the sheared sample is placed, normal load hydraulic piston above the upper deck. **B**, The numerical model of the shearing samples for temperature simulation; shown as cross section of both blocks. **C**, Close-up view of a Sierra White granite sample block assembled in the loading frame; note the raised ring of the upper block and two thermocouples at 3 and 6 mm from the sliding surface. After (Reches and Lockner, 2010).

Table A1
Experimental conditions and HARD friction law parameters.

Run#	σ_N (MPa)	Max velocity (m/s)	Rise time (s)	VT[a] (m)	Accel[b] (m/s²)	D_H	D_W	D_T	μ_O	μ_S	μ_K	μ_F	Mode[c]
711	2	0.25	3.4	0.85	5.2	0.003	0.015	0.42	0.411	0.62	0.36	0.62	Pulse
712	2	0.24	3.4	0.816	6.1	0.003	0.015	0.43	0.53	0.64	0.33	0.57	Pulse
733	6.8	0.7	2.5	1.75	28.8	0.006	0.047	0.87	0.67	0.68	0.34	0.81	Pulse
742	3.7	0.51	3	1.53	26.1	0.005	0.034	0.74	0.729	0.76	0.35	0.78	Pulse
743	3.7	0.39	2.1	0.819	21.7	0.01	0.026	0.37	0.736	0.76	0.5	0.74	Pulse
2782	2.23	0.79	3.5	2.765	3.2	0.044	0.076	1.5	0.75	0.74	0.27	0.74	Pulse
2784	2.28	0.94	3.34	3.1396	4	0	0.1	1.79	0.82	0.79	0.2	0.74	Pulse
2783	2.26	0.8	5.7	4.56	0.26	0.05	0.39	5.7	0.74	0.74	0.49	0.8	Gaussian
2785	2.3	1	6.4	6.4	0.32	0.043	0.45	3.46	0.77	0.79	0.35	0.84	Gaussian
3071	2.55	0.8	3.5	2.8	0.23	0.089	0.14	1.37	0.58	0.63	0.56	0.73	Gaussian
3072	2.62	0.73	3.7	2.701	0.23	0.11	0.25	1.34	0.65	0.73	0.59	0.76	Gaussian
2752	2.35	0.27	11.4	3.078	0	0.09	0.11	2.5	0.74	0.84	0.68	0.74	Gaussian
727	2.3	0.21	1.8	0.378	13.7		0.037	0.15		0.65	0.63		No Weak
725	2.3	0.1	0.9	0.09	8.3			0.04		0.61	0.61		No Weak
741	3.7	0.25	1.2	0.3	17.1			0.13		0.7	0.7		No Weak
2854	6.56	0.096	2.47	0.2371	0			2.44		0.7	0.74	0.75	No Weak

Comments:
[a] VT = maximum velocity x rise time.
[b] Accel = mean slip acceleration.
[c] See modes of slip in Figs. 3.

Appendix A. Experimental setup

The analyzed experiments were conducted with the Rotary Shear Gouge Apparatus (ROGA) apparatus at the University of Oklahoma (Chang et al., 2012; Reches and Lockner, 2010; Liao et al., 2014) (Fig. A1). The apparatus' capabilities include: (1) normal stress up to 30 MPa; (2) slip velocity 0.0003-2 m/s; (3) rise-time of less than 1 s; and (4) unlimited slip distances. The experimental faults were composed of solid blocks of Sierra White and Radiant Red granites (Chen et al., 2017a). Each sample includes two cylindrical blocks, diameter = 101.6 mm, height = 50.8 mm. The upper block has a raised ring of ID = 63.2 mm and OD = 82.3 mm; the blocks are pressed across this raised ring. Thermocouples are cemented into holes drilled 3 mm away from the sliding surfaces (Fig. A1C). Apparatus control and data monitoring are conducted with a dedicated LabView program at frequency of 100-5,000 Hz.

Appendix B. Numerical simulation of dynamic rupture

The present simulations utilized the SCEC-USGS benchmark model version 3 (Moczo et al., 2007; Rojas, et al., 2008; Pelties et al., 2012; http://scecdata.usc.edu/cvws/benchmark_descriptions.html). This model is for of a vertical strike-slip fault (Fig. 4C), the properties of which can be modified by the modeler, including:

Table A2

Model properties of SCEC-USGS version 3 benchmark model for rupture simulation (Rojas et al., 2008). Values underlined are modified in present analysis and the modified values for HARD friction laws are in Table A3.

Parameters	Nucleation patch on the fault	Fault surface outside nucleation	Medium surrounding the fault
Initial shear stress τ_0, MPa	81.6	70	70
Initial normal stress $-\sigma_n$, MPa	120	120	120
Static friction coefficient μ_s	0.677	0.677	Infinite
Dynamic friction coefficient μ_K	0.525	0.525	0.525
Static yielding stress $\tau_s = -\mu_s\sigma_n$, MPa	81.24	81.24	Infinite
Dynamic yielding stress $\tau_d = -\mu_K\sigma_n$, MPa	63	63	63
Dynamic stress drop $\Delta\tau = \tau_0 - \tau_K$, MPa	18.6	7	7
Strength excess $\tau_s - \tau_0$, MPa	−0.36	11.24	Infinite

Table A3

The parameters of HARD law used for in the simulations (Figs. 4, 6).

Parameters	Case 1	Case 2	Case 3	Case 4	Gorkha
Initial friction coefficient μ_0	0.677	0.677	**0.474-0.677**	0.677	0.677
Static friction coefficient μ_S	0.677	0.677	0.677	0.677	0.677
Dynamic friction coefficient μ_K	0.525	0.525	0.525	0.525	0.525
Final friction coefficient μ_F	0.677	0.677	0.677	**0.525-0.677**	**0.677**
Initial strengthening distance D_H, m	0.00003	0.0005	0.05	0.05	0.0005
Slip weakening distance D_W, m	**0.033-0.235**	**0.1-0.7**	0.5	0.5	0.5
Total slip-distance D_T, m	0.5	1.5	1.5	1.5	1.5

fault geometry, friction law, constitutive parameters, nucleation process, medium elastic and strength properties, and the boundary conditions.

Considering a homogeneous, linear elastic continuum with a Cartesian co-ordinate system $y = 0$, the elastodynamic relations between tractions and displacement discontinuities on the fault plane, can be expressed as equation (3) (Geubelle and Rice, 1995; Morrissey and Geubelle, 1997). The numerical implementation of boundary integral method has been widely used to investigate spontaneous ruptures within an elastic continuum (Andrews, 1985; Geubelle and Rice, 1995; Morrissey and Geubelle, 1997; Lapusta et al., 2000; Ampuero and Vilotte, 2002; Day and Dalguer, 2005). The SBIEM code solves for the slip and evolving stress on the fault plane as the rupture progresses, expressing the elastodynamic response of the elastic continuum in terms of integral relationships of displacement and tractions (Ampuero and Vilotte, 2002; Day and Dalguer, 2005). The convolutions kernel in space and time is provided and validated to eliminate the necessity to simulate the wave propagation through elastic continuum by assuming an infinite, uniform elastic solid (Morrissey and Geubelle, 1997). In this numerical scheme, the rupture problem becomes computationally intensive, precise and flexible. This method has been used and discussed to simulate crack propagations using slip-weakening or rate- and state-dependent friction laws (Lapusta et al., 2000).

We use the SBIEM code to investigate the effects of the HARD friction law on the propagation of a dynamic rupture along a fault that is embedded in a homogeneous, infinite, elastic medium (Fig. 4C). The medium properties (Table A2) include P and S wave velocities of 6 km/s and 3,464 m/s, respectively, and density of 2,670 km/m^3. The vertical fault in the x-z plane that is 30 km long in the z direction and 15 km long in the x direction with a 3 km long nucleation patch in its center (Fig. 4C). The model is subjected to shear stress parallel to the fault (Fig. 4B). The nucleation patch is subjected to higher shear stress than the fault surface outside the nucleation patch (Table A2), thus it will fail first, and the dynamic rupture will propagate along the fault in x and z directions. The surrounding elastic medium around the fault is set to be too strong to fail and reacts elastically to the fault slip (Moczo et al., 2007; http://scecdata.usc.edu/cvws/benchmark_descriptions.html; Fig. 5B). In this configuration, the rupture properties are monitored along the x-axis (Fig. 4C), up to a distance of

7.5 km from the center. Initial stresses and median properties are presented in Table A2 and HARD friction in Table A3.

References

Ampuero, J.P., Vilotte, J.P., 2002. Nucleation of rupture under slip dependent friction law: simple models of fault zone. J. Geophys. Res. 107 (B12). https://doi.org/10.1029/2001JB000452.

Andrews, D.J., 1985. Dynamic plane-strain shear rupture with a slip-weakening friction law calculated by a boundary integral method. Bull. Seismol. Soc. Am. 75 (1), 1–21.

Barall, M., Harris, R.A., 2015. Metrics for comparing dynamic earthquake rupture simulations. Seismol. Res. Lett. 86 (1), 223–235.

Bizzarri, A., Cocco, M., 2003. Slip-weakening behavior during the propagation of dynamic ruptures obeying rate-and state-dependent friction laws. J. Geophys. Res., Solid Earth 108 (B8), 2373. https://doi.org/10.1029/2002JB002198.

Brace, W.F., Byerlee, J.D., 1966. Stick-slip as a mechanism for earthquakes. Science 153, 990–992.

Chang, J.C., Lockner, D.A., Reches, Z., 2012. Rapid acceleration leads to rapid weakening in earthquake-like laboratory experiments. Science 338, 101–105.

Chen, X., Madden, A.S., Bickmore, B.R., Reches, Z., 2013. Dynamic weakening by nanoscale smoothing during high-velocity fault slip. Geology 41, 739–742.

Chen, X., Madden, A.S.E., Reches, Z., 2017a. Powder rolling as a mechanism of dynamic fault weakening. In: Thmas, M.Y., Mitchell, T.M., Bhat, H.S. (Eds.), Fault Zone Dynamic Processes: Evolution of Fault Properties During Seismic Rupture. In: Geophysical Monograph Series, pp. 133–150.

Chen, X., Elwood Madden, A.S., Reches, Z., 2017b. Friction evolution of granitic faults: heating controlled transition from powder lubrication to frictional melt. J. Geophys. Res., Solid Earth 122, 9275–9289.

Dascalu, C., Ionescu, I., Campillo, M., 2000. Fault finiteness and initiation of dynamic shear instability. Earth Planet. Sci. Lett. 177, 163–176.

Day, S., Dalguer, L.A., 2005. Comparison of finite difference and boundary integral solutions to three-dimensional spontaneous rupture. J. Geophys. Res. 110 (B12). https://doi.org/10.1029/2005JB003813.

Di Toro, G., Goldsby, D.L., Tullis, T.E., 2004. Friction falls toward zero in quartz rock as slip velocity approaches seismic rates. Nature 427, 436–439.

Di Toro, G., Han, R., Hirose, T., De Paola, N., Nielsen, S., Mizoguchi, K., Ferri, F., Cocco, M., Shimamoto, T., 2011. Fault lubrication during earthquakes. Nature 471, 494–498.

Dieterich, J.H., 1979. Modeling of rock friction: 1. Experimental results and constitutive equations. J. Geophys. Res. 84 (B5), 2161–2168.

Fukuyama, E., Mizoguchi, K., 2010. Constitutive parameters for earthquake rupture dynamics based on high-velocity friction tests with variable slip rate. Int. J. Fract. 163, 15–26.

Galetzka, J., Melgar, D., Genrich, J.F., et al., 2015. Slip pulse and resonance of the Kathmandu basin during the 2015 Gorkha earthquake, Nepal. Science 349, 1091–1095.

Geubelle, P.H., Rice, J.R., 1995. A spectral method for three-dimensional elastodynamic fracture problems. J. Mech. Phys. Solids 43, 1791–1824.

Goldsby, D.L., Tullis, T., 2011. Flash heating leads to low frictional strength of crustal rocks at earthquake slip rates. Science 334 (6053), 216–218.

Green II, H.W., Shi, F., Bozhilov, K., Xia, G., Reches, Z., 2015. Phase transformation and nanometric flow cause extreme weakening during fault slip. Nat. Geosci. 8 (6), 484.

Han, R., Shimamoto, T., Hirose, T., Ree, J.H., Ando, J., 2007. Ultralow friction of carbonate faults caused by thermal decomposition. Science 316, 878–881.

Heaton, T.H., 1990. Evidence for and implications of self-healing pulses of slip in earthquake rupture. Phys. Earth Planet. Inter. 64, 1–20.

Hirose, Takehiro, Shimamoto, T., 2005. Slip-weakening distance of faults during frictional melting as inferred from experimental and natural pseudotachylytes. Bull. Seismol. Soc. Am. 95, 1666–1673.

Ida, Y., 1972. Cohesive force across the tip of a longitudinal shear crack and Griffith's specific surface energy. J. Geophys. Res. 77, 3796–3805.

Ide, S., Takeo, M., 1997. Determination of constitutive relations of fault slip based on seismic wave analysis. J. Geophys. Res. 102 (B12), 27379–27391.

Jiang, J., Lapusta, N., 2016. Deeper penetration of larger earthquakes on seismically quiescent faults. Science 352 (6291), 1293–1297.

Kanamori, H., Brodsky, E.E., 2004. The physics of earthquakes. Rep. Prog. Phys. 67, 1429.

Lapusta, N., Rice, J.R., Ben-Zion Zheng, Y.G., 2000. Elastodynamic analysis for slow tectonic loading with spontaneous rupture episodes on faults with rate- and state-dependent friction. J. Geophys. Res. 105, 23765–23789.

Liao, Z., Chang, J.C., Reches, Z., 2014. Fault strength evolution during high velocity friction experiments with slip-pulse and constant-velocity loading. Earth Planet. Sci. Lett. 406, 93–101.

Marone, C., 1998. Laboratory-derived friction laws and their application to seismic faulting. Annu. Rev. Earth Planet. Sci. 26, 643–696.

Moczo, P., Kristek, J., Galis, M., Pazak, P., Balazovjech, M., 2007. The finite-difference and finite-element modeling of seismic wave propagation and earthquake motion. Acta Phys. Slovaca 57 (2), 177–406.

Morrissey, J.W., Geubelle, P.H., 1997. A numerical scheme for mode III dynamic fracture problems. Int. J. Numer. Methods Eng. 40, 1181–1196.

Noda, H., Lapusta, N., 2010. Three-dimensional earthquake sequence simulations with evolving temperature and pore pressure due to shear heating: effect of heterogeneous hydraulic diffusivity. J. Geophys. Res., Solid Earth 115 (B12). https://doi.org/10.1029/2010JB007780.

Ohnaka, M., Yamashita, T., 1989. A cohesive zone model for dynamic shear faulting based on experimentally inferred constitutive relation and strong motion source parameters. J. Geophys. Res. 94, 4089–4104.

Olsen, K.B., Madariaga, R., Archuleta, R.J., 1997. Three-dimensional dynamic simulation of the 1992 Landers earthquake. Science 278 (5339), 834–838.

Palmer, A.C., Rice, J.R., 1973. The growth of slip surfaces in the progressive failure of over-consolidated clay. Proc. R. Soc. Lond. Ser. A, Math. Phys. Sci. 332, 527–548.

Pelties, C., de la Puente, J., Ampuero, J.-P., Brietzke, G.B., Kaeser, M., 2012. Three-dimensional dynamic rupture simulation with a high-order discontinuous Galerkin method on unstructured tetrahedral meshes. J. Geophys. Res. 117 (B2). https://doi.org/10.1029/2011JB008857.

Reches, Z., Dewers, T.A., 2005. Gouge formation by dynamic pulverization during earthquake rupture. Earth Planet. Sci. Lett. 235, 361–374.

Reches, Z., Lockner, D.A., 2010. Fault weakening and earthquake instability by powder lubrication. Nature 467, 452–455.

Rice, J.R., 2006. Heating and weakening of faults during earthquake slip. J. Geophys. Res. 111, B5. https://doi.org/10.1029/2005JB004006.

Rojas, O., Day, S., Castillo, J., Dalguer, L.A., 2008. Modelling of rupture propagation using high-order minetic finite differences. Geophys. J. Int. 172, 631–650.

Scholz, C.H., 2002. The Mechanics of Earthquakes and Faulting. Cambridge Univ. Press, New York.

Siman-Tov, S., Aharonov, E., Boneh, Y., Reches, Z., 2015. Fault mirrors along carbonate faults: formation and destruction during shear experiments. Earth Planet. Sci. Lett. 430, 367–376.

Sone, H., Shimamoto, T., 2009. Frictional resistance of faults during accelerating and decelerating earthquake slip. Nat. Geosci. 2, 705–708.

Spagnuolo, E., Nielsen, S., Violay, M., Di Toro, G., 2016. An empirically based steady state friction law and implications for fault stability. Geophys. Res. Lett. 43, 3263–3271.

Svetlizky, I., Fineberg, J., 2014. Classical shear cracks drive the onset of dry frictional motion. Nature 509, 205–208.

Tinti, E., Fukuyama, E., Piatanesi, A., Cocco, M., 2005. A kinematic source-time function compatible with earthquake dynamics. Bull. Seismol. Soc. Am. 95, 1211–1223.

Viesca, R.C., Garagash, D.I., 2015. Ubiquitous weakening of faults due to thermal pressurization. Nat. Geosci. 8, 875–879.

Wald, D.J., 1996. Slip history of the 1995 Kobe, Japan, earthquake determined from strong motion, teleseismic, and geodetic data. J. Phys. Earth 44 (5), 489–503.

Weng, H., Yang, H., 2018. Constraining frictional properties on fault by dynamic rupture simulations and near-field observations. J. Geophys. Res. 123 (8), 6658–6670.

Wilson, B., Dewers, T., Reches, Z.E., Brune, J., 2005. Particle size and energetics of gouge from earthquake rupture zones. Nature 434 (7034), 749.